A Reanalysis of the MSU Channel 2 Tropospheric Temperature Record

CARL A. MEARS, MATTHIAS C. SCHABEL, AND FRANK J. WENTZ

Remote Sensing Systems, Santa Rosa, California

ABSTRACT

Over the period from 1979 to 2001, tropospheric trends derived from a widely cited analysis of the Microwave Sounding Unit (MSU) temperature record show little or no warming, while surface temperature trends based on in situ observations show a pronounced warming of $\sim$0.2 K decade^{-1}. This discrepancy between trends at the surface and in the upper atmosphere has been a source of significant debate. Model predictions of amplification of warming with height in the troposphere are clearly inconsistent with the available observations, leading some researchers to question the adequacy of their representation of the water vapor greenhouse feedback. A reanalysis of the MSU channel 2 dataset, with the objective of providing a second independent source of these data, is described in this paper. Results presented herein show a global trend of 0.097 $\pm$ 0.020 K decade^{-1}, generally agreeing with the work of Prabhakara et al. but in disagreement with the MSU analysis of Christy and Spencer, which shows significantly less ($\sim$0.09 K decade^{-1}) warming. Differences in the various methodologies are discussed and it is demonstrated that the principal source of these discrepancies is in the treatment of errors due to variations in the temperature of the MSU hot calibration target.

1. Introduction

Researchers generally agree that the surface warming observed over the past century is at least partially anthropogenic in origin, particularly that seen in the past two decades (Hansen et al. 2001; Houghton et al. 2001). In the upper atmosphere the situation is significantly less clear due to the relative paucity and short time period of observations (Hurrell et al. 2000). Radiosondes, the principal tool for atmospheric profiling, have limited spatial coverage, particularly over large portions of the oceans, and are subject to a host of complications, including changing instrument types, configurations, and observation practices (Gaffen et al. 2000; Lanzante et al. 2003a,b), making long-term climatological studies difficult. While the advent of temperature sounding microwave radiometers flown on National Oceanic and Atmospheric Administration (NOAA) polar-orbiting weather satellites provided a new and complementary source of upper-atmosphere observations beginning with *TIROS-N* in 1978 and continuing through the present, the Microwave Sounding Unit (MSU), and the follow-on instrument, the Advanced Microwave Sounding Unit (AMSU), were designed primarily for meteorological rather than climatological purposes. Despite excellent coverage (more than half the earth's surface daily), the MSU data suffer from a number of calibration issues and time-varying biases that must be addressed if they are to be used for climate change studies.

The MSU instruments have four channels spanning the frequency range from 50.2992 to 57.9499 GHz. Thermal emission from atmospheric oxygen constitutes the major component of the measured brightness temperature, with the vertical weighting profile varying from near the surface in channel 1 to the stratosphere in channel 4. In this work, we focus on MSU channel 2 at 53.74 GHz. About 80% of the signal for this channel comes from the troposphere, with the weighting function peaking from 4 to 7 km above the surface, depending on earth incidence angle. The remainder of the signal comes from the surface and stratosphere, with the exact contribution of each dependent on the surface type and the atmospheric profile at the point of measurement. While other workers have attempted to increase the sensitivity of the MSU channel 2 (MSU2) measurements to the lower troposphere by employing a differencing scheme to extrapolate the measurements downward to produce the so-called MSU2LT data, (Spencer and Christy 1992b, Christy et al. 2003, and references therein) this approach amplifies noise and introduces other complications. For this reason, we have chosen to focus on the raw channel 2 data.

Initial studies of the midtroposphere MSU channel 2 data performed by Christy and Spencer (Christy and Spencer 1995; Christy et al. 1998, 2000, 2003; Spencer and Christy 1990, 1992a,b) uncovered a number of important sources of error in those data, including intersatellite offsets, the significance of diurnal warming

Corresponding author address: Carl A. Mears, 438 First St., Ste. 200, Santa Rosa, CA 95401.
E-mail: mears@remss.com

with slow evolution in the satellite local equator crossing times (LECT), and the presence of a significant correlation between observed intersatellite brightness temperature differences and satellite hot calibration load temperature. Impacts of these various contributions were gradually identified and corrected in successive versions of their merged dataset, with resulting long-term trends cooling relative to the surface, particularly in the Tropics and subtropics. These results, combined with the even more rapid cooling in MSU2LT, sparked an intense debate centered on their inconsistency with general circulation model predictions and many surface datasets (Hansen et al. 1995; Santer et al. 1999, 2000; Wallace et al. 1999).

Drawing on work by Trenberth and Hurrell (1997), an investigation of systematic correlations in the MSU2/MSU2LT time series by Wentz and Schabel (1998) revealed the presence of a spurious cooling trend introduced into the MSU2LT data by neglect of the differential effects of satellite orbit decay on the near-limb and near-nadir observations. Accounting for this led to an increase in the global trend of approximately 0.12 K decade^{-1}, bringing the lower-troposphere observations more in line with model predictions and surface measurements. Christy and Spencer subsequently argued for the presence of additional diurnal and target temperature contributions that largely offset the orbit decay effect, again leading to a surface–troposphere disconnect (Christy et al. 2000). Prabhakara et al. (1998, 2000) also performed an independent analysis of the MSU dataset, but their analysis uses a simplified model for the effects of the calibration target temperature compared to that used either in Christy et al. (2000, 2003) or the present analysis; thus, it is difficult to assess the validity of their approach.

The significance of the MSU dataset in climate change research, and the possibility of systematic errors in it, inspired the complete reanalysis described herein. We have developed a completely independent dataset based solely on the raw MSU channel 2 observations. This analysis is complementary to that of Christy and Spencer and provides the opportunity to compare and contrast the effects of various corrections on the overall time series and to elucidate the origins of discrepancies between the two.

Data presented in this paper were derived from a comprehensive reanalysis of the raw level 0 count data for all nine MSU instruments beginning with *TIROS-N* and ending with *NOAA-14.* Doing this ensures that there are no common dependencies between our analysis and that of Christy and Spencer (hereafter CS), and serves as a useful double check of our methodology in its entirety. In section 2 we briefly describe the preliminary calibration steps and quality control procedures involved in producing individual brightness temperature series for each instrument. Section 3 addresses techniques for characterization and removal of incidence angle variations and the diurnal variation of temperature. The in-

volved and critical question of how to intercalibrate observations from different instruments in a consistent way is treated in section 4, including a discussion of error estimates and correlations. We present results for long-term global and spatially resolved trends in section 5, comparing them with the corresponding quantities from the CS analysis. Section 6 details the principal aspects of the methodologies that we believe account for most of the observed discrepancies between our data and the Christy and Spencer data. A summary is provided in section 7.

2. Preliminary quality control

Preprocessing of the level 0 (raw counts) MSU data involves a number of quality control and calibration steps, which are briefly described here. Much of the necessary information on data format and calibration is found in the NOAA Polar Orbiter Description (POD) document (Kidwell 1998). Here we focus on two primary elements of the quality control procedure: first, validation of the supplied geolocation data, and second, production of calibrated brightness temperatures from the supplied raw counts.

Our geolocation quality control procedure utilizes orbital two-line elements (TLEs) provided by the National Aeronautics and Space Administration's (NASA) Orbital Information Group (OIG) in conjunction with a satellite orbital propagation model and a geometrical model of the MSU instrument itself to generate predicted geolocation data (Hoots and Roehrich 2003). We use these predicted values to perform a basic check on the geolocation values provided by National Environmental Satellite, Data, and Information Service (NESDIS), rejecting any footprints for which the distance between predicted and provided earth locations exceed the width of a footprint or for which the nadir angle deviates from nominal by more than 1°. At the same time, due to highly unreliable satellite orbital altitude data prior to 1994, we use the orbit propagator to generate exact orbit heights, enabling precise compensation in the final dataset for instantaneous altitude variations as well as long-term secular orbit decay effects (Wentz and Schabel 1998).

Basic brightness temperature conversion and calibration is performed by converting raw counts to corrected counts using coefficients that account for radiometer nonlinearities determined using prelaunch calibration measurements. Then the earth scene counts are converted to a temperature using the hot-load and cold-space counts, and the measured hot-load temperature, using a linear two-point calibration method. Our final analysis relies on the nominal, NOAA-supplied, calibration coefficients, except for *NOAA-12,* which utilizes the reconstructed data from Mo (1995). We performed additional checks using both simple linear calibration (no nonlinearity correction) and the more recent (Mo et al. 2001) calibration coefficients and found essentially

no difference in the final intercalibrated brightness temperature data. This is presumably due to our incorporation of radiometric nonlinearities in the empirical target factor term discussed in detail in section 4. Histograms of observed brightness temperatures were accumulated for each satellite and visually inspected to determine appropriate quality control cutoff values. Excepting occasional periods of bad data, the quality control procedure eliminates approximately 0.1% of the observations.

3. Preprocessing of brightness temperature data

Once the individual observations have been processed, but before the MSU channel 2 brightness temperatures can be merged into a single time series, two important adjustments must be made to remove biases and long-term drifts in the record from each individual instrument.

a. Incidence angle correction

The MSU instruments are cross-track scanners that measure the upwelling microwave radiance for 11 views with corresponding incidence angles ranging from 0° to 56°. To remove long-term effects due to slow, time-dependent decay in the spacecraft's altitude, and to reduce ''sampling noise'' that occurs when averaging different numbers of measurements from different fields of view (FOVs) together, we correct each measurement to an equivalent nadir view, compensating for the slight differences in the vertical weighting profile between incidence angles. Correction to nadir is accomplished by computing simulated brightness temperatures both at the observed earth incidence angle (EIA) and at nadir, and then adding the difference of these to the measured T_b. Simulated brightness temperatures were calculated using interpolated mean monthly National Centers for Environmental Prediction (NCEP) surface and atmospheric profiles from 1996 on a 2.5° rectangular grid as input to a well-calibrated radiative transfer model (Wentz and Meissner 1999). Ocean emissivity was determined using a detailed ocean surface model that includes the effects of wind-induced surface roughness and the variation of emissivity with sea surface temperature, while land emissivity was assumed to be fixed. While the constant land emissivity assumption is not necessarily a good one, particularly in regions having snow and ice cover or significant variations in land cover or soil moisture, the low sensitivity of the MSU channel 2 observations to the surface (1%–10%, depending on EIA and topographic elevation) and the fact that we are applying a derivative correction makes this a small second-order effect.

In addition to secular variation in incidence angle due to satellite orbit decay and small periodic fluctuations in EIA over the course of an orbit, we also noted large, consistent biases between fields of view on opposite
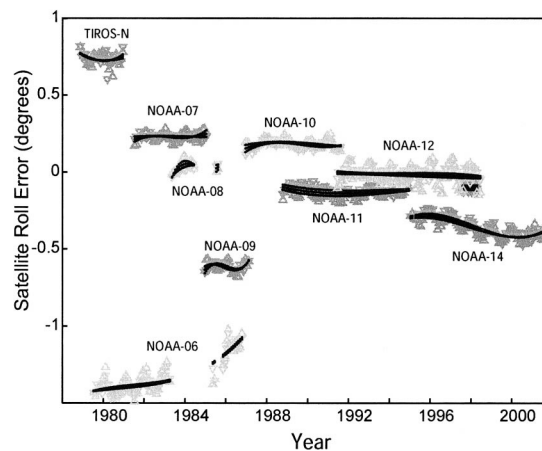

FIG. 1. Time series of retrievals, for each satellite for MSU channel 2. The colored symbols are the retrieved rolls, and the black crosses are the results of a polynomial fit to the time dependence of the roll error. Other than the anomalous time dependence of the *NOAA-6* bias and a slight trend in *NOAA-14,* the roll errors are nearly constant in time.

sides of the swath in the observations from some instruments. These biases vary in both sign and magnitude between platforms and are generally largest in the early members of the series, and could stem from a number of sources including misalignment of the entire instrument or the beam-directing mirror, or asymmetric distortions of the beam pattern. While their exact origin is difficult to establish, they can be well modeled as an instrumental attitude roll. The effective roll angle needed to remove the cross-swath bias is calculated using a least squares fit to global observations averaged over 3-month periods, with the resulting roll angle used to adjust both land and ocean measurements. The results of the roll regressions are presented in Fig. 1. While there are small seasonal variations in the roll series for all satellites, noticeable trends are only apparent in *NOAA-6* at the end of its operational lifetime and, to a lesser degree, in *NOAA-14*. The low-frequency time dependence of the roll error is separated from the small seasonal-scale fluctuations arising from model errors in the simulated seasonal cycle by using a third-order polynomial regression to the time series of derived roll errors. Once the time dependence of the roll has been determined, it is removed from each MSU footprint individually based on the simulated NCEP value, interpolated to spatially and temporally coincide with the actual observation. In Fig. 2, we show the results of the incidence angle correction for the January averaged *NOAA-6* data. Both the cross-scan asymmetry and the difference between the outer and inner scans have been dramatically reduced. Similar plots for the other satellites reveal comparable improvement. Since we use combinations of MSU views that are symmetric around the nadir view, any error in these adjustments does not cause significant changes in our long-term time series.
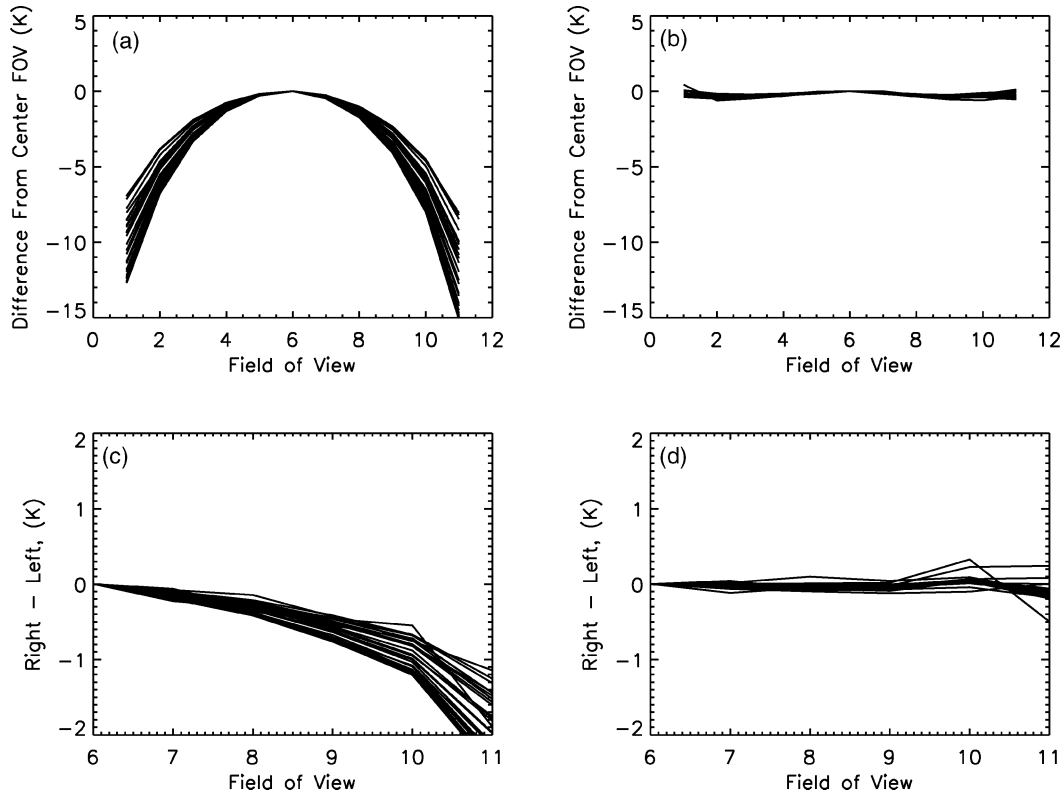
FIG. 2. Example of incidence angle adjustment. (a) Zonal averaged differences between all measurements in a given field of view and the central field of view are plotted. Each line corresponds to the average over a 5° zonal band, starting at 75°S and finishing at 75°N. This plot is created by averaging all *NOAA-6* measurements made during the month of Jan. Note the asymmetry between the right and left sides of the scan. (c) To highlight this asymmetry, the difference between a given field of view, and its corresponding field of view on the opposite side of the scan, are plotted. (b), (d) Plots corresponding to the same data as in (a), (c) but after we apply our incidence angle adjustment, referring each measurement to the nadir view, and taking into account the retrieved effective roll from Fig. 1.

b. Diurnal correction

All of the MSU instruments exhibit the slow drift in local equator crossing time shown in Fig. 3. The principal effect of this drift is to introduce a slow variation in the local time observed by the instrument. This drift in sampling time will cause aliasing of any diurnal signal present into the long-term time series, potentially introducing a spurious trend in the measured T_b. It is important to note that, while the observations fro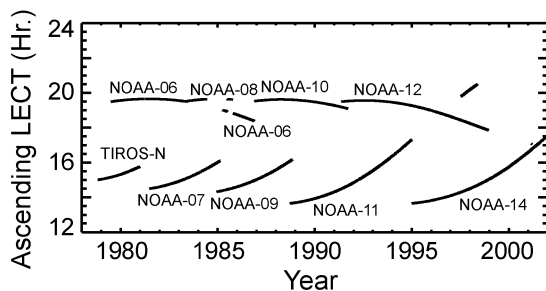m only ascending or from only descending passes will be dramatically affected by such large changes in LECT, their average will tend to cancel out. In particular, if we decompose the diurnal temperature signal into a Fourier series, the terms arising from the odd harmonics cancel completely at the equator, due to the 12-h time difference between observations, and approximately elsewhere. This insensitivity to the dominant first harmonic term is fortuitous in the sense that it minimizes the absolute magnitude of the diurnal effect, but at the same time places stringent requirements on the accuracy of the estimation of the shape of the diurnal cycle prior to removing it from the data.

In order to sidestep some of the difficulties encountered in attempting to characterize the diurnal cycle entirely based on the observed data, we developed a method (Mears et al. 2002) based on hourly output from a 5-yr run of the National Center for Atmospheric Research's (NCAR) Community Climate Model (CCM3; Kiehl et al. 1996) to calculate a climatology of local diurnal anomalies in the brightness temperature for each of the six distinct view angles measured by the MSU instrument. Recording the model results on an hourly timescale enables us to resolve the shape of the diurnal
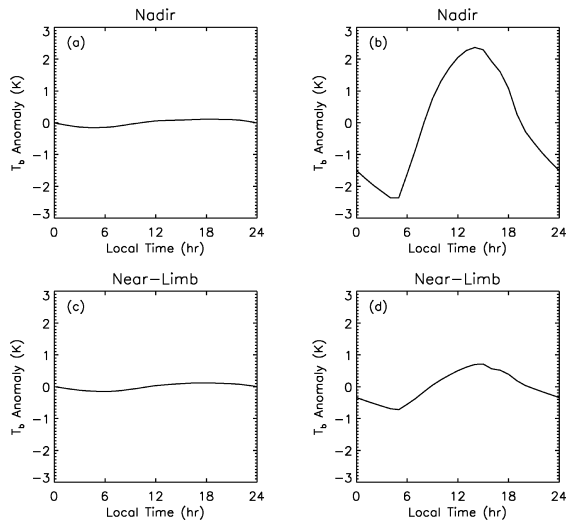

FIG. 3. Ascending node LECT for each MSU instrument.

FIG. 4. Simulated MSU channel 2 diurnal cycles calculated from hourly CCM3 output for the month of Jun. (a), (c) A 2.5° × 2.5° box in the tropical Pacific, centered at 1.25°N, 178.75°W. (b), (d) A 2.5° × 2.5° box in the western United States, centered at 38.75°N, 113.75°W.
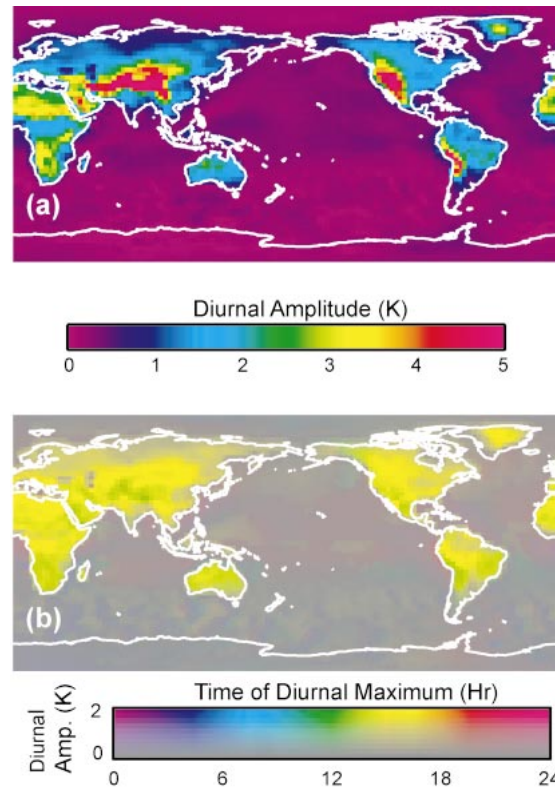

FIG. 5. (a) Mean simulated MSU channel 2 diurnal peak-to-peak amplitude for Jun at the nadir view. (b) Mean local time of simulated diurnal maximum, with the amplitude of the diurnal cycle denoted by the saturation of the color. (This is done so the reader is not confused by anomalous diurnal maxima caused by noise in regions with small diurnal amplitude.)

cycle through the fourth harmonic, the importance of which is discussed above.

Gridded climatologies of hourly/monthly simulated MSU channel 2 brightness temperatures for each of the six distinct MSU FOVs were generated using the CCM3 atmospheric profiles and surface variables in conjunction with our microwave radiative transfer and surface emissivity models (Wentz and Meissner 1999). Over the oceans, we use the comprehensive surface model mentioned above, while over land, we assume a constant emissivity of 0.95, a typical value for dry, vegetated regions.

In Fig. 4 we show characteristic diurnal cycles for the month of June in two locations representing extremes in observed diurnal behavior. Figures 4a and 4c show the diurnal cycle over a grid point in the western tropical Pacific for the nadir and near-limb views, respectively. These two cases reveal small amplitudes and similar shapes dominated by the first harmonic, suggesting a diurnal cycle that arises from heating throughout the troposphere. We find that these features are characteristic of the diurnal behavior over virtually all ocean surfaces, a result consistent with recent microwave sea surface temperature (SST) measurements by Gentemann et al. (2003) showing that the diurnal cycle amplitude in the ocean skin layer temperature is typically less than 0.5 K. The net effect of such small, largely sinusoidal diurnal cycles on the long-term time series of combined ascending and descending node measurements is minimal.

Figures 4b and 4d are for a land location in the western United States. Large summer surface warming in this desert location combines with the relatively dry atmosphere and high elevation to produce a large diurnal

signal in the simulated brightness temperatures. There is significant reduction in amplitude of the near-limb view relative to the nadir view, indicating that a significant portion of the observed diurnal cycle is due to surface warming, which is attenuated by the longer path through the atmosphere in the near-limb view, rather than heating of the upper atmosphere itself.

Figure 5 shows maps of the diurnal amplitude and the local time of diurnal maximum for the month of June at nadir. We observe that the simulated diurnal cycle has its largest amplitudes in high-altitude regions, where the surface is less obscured by atmospheric absorption, and in dry regions, which have large near-surface diurnal cycles arising from the interplay between direct solar heating in the day and radiative cooling at night. In contrast, the diurnal amplitude is much smaller in low-altitude, heavily vegetated land regions and over the ocean where the higher heat capacity tends to dampen day–night variation. In the regions with the largest amplitudes, the brightness temperature peaks shortly after local noon, while land regions with smaller amplitudes show a delayed peak a few hours later. Low- and midlatitude ocean regions tend to peak even later in the
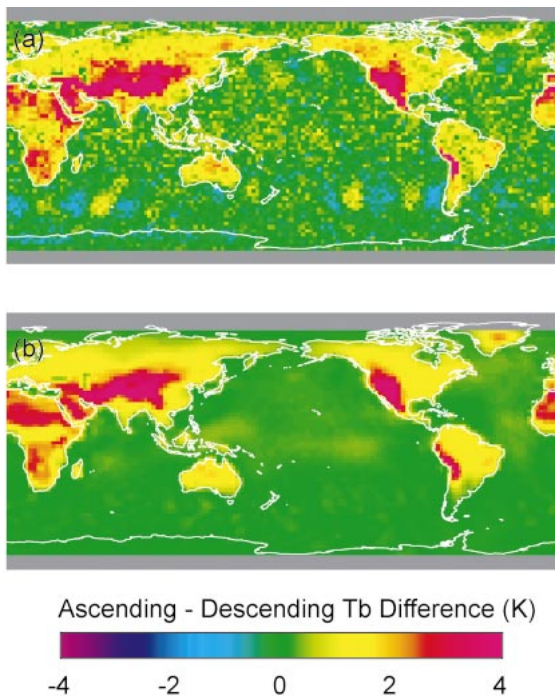
FIG. 6. (a) Ascending–descending channel 2 brightness temperature differences for the entire MSU dataset for the central five FOVs, the month of Jun, and for ascending node equatorial crossing times between 1500 and 1600 LT. The roughly periodic variation visible in the southern oceans is due to nonuniform sampling of the seasonal cycle. (b) Same as in (a) except simulated using the CCM3 diurnal climatology.
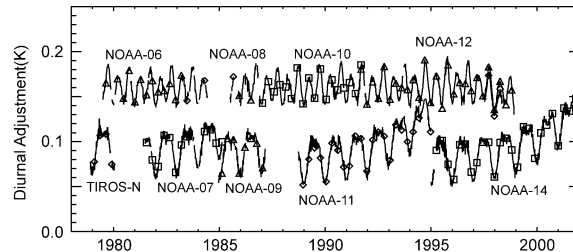

FIG. 7. Effect of the diurnal correction on global pentads. Each line is a plot of the difference between global 5-day averages with and without the diurnal correction applied. Symbols are plotted at periodic intervals to help the reader identify which line represents each satellite in regions where they overlap.

day, though the significance of this is unclear given the vastly reduced amplitude of the signal.

Prior to correction of the long-term time series of MSU brightness temperatures for diurnal drift, we validate our diurnal model by comparing collocated observations of ascending–descending brightness temperature differences (separated by ~12 h near the equator; ~10 h at 65°N or 65°S) with the corresponding simulated differences from the model data. Differences are computed by binning the incidence angle corrected brightness temperatures, averaged over the central five fields of view, by hour of local equator crossing time, with similar histograms formed from the simulation data.

Figure 6 compares the measured and simulated ascending–descending differences for the 1530 LT bin for the month of June. The good quantitative agreement between the patterns and amplitudes gives us confidence that the CCM3 model represents the diurnal cycle with sufficient accuracy to be of use in developing a correction. Comparisons of the ascending–descending differences for other crossing time bins and months show similar agreement. Correlation coefficients between the measured and simulated maps (spatially smoothed with a boxcar smoother of width 22.5° to reduce sampling noise) are generally above 0.8. The most apparent model

inaccuracies are a slight overestimation of the diurnal cycle over tropical forests (visible in tropical Africa and the Amazon basin) and a slight underestimation of the diurnal cycle in some high-latitude land areas (visible in northwestern Canada and eastern Siberia), possibly due to our assumption of constant land surface emissivity. Except in the dense rain forest, our value of 0.95 is probably an overestimate; also, seasonally varying snow cover and soil moisture have a large time-varying effect on emissivity and on the vertical weighting function (Shah and Rind 1995). Future refinement of this dataset will include an improved land surface emissivity model.

Using the diurnal climatology simulated from CCM3, we adjust all MSU measurements to the same local time so that drifts in the measurement time no longer affect any deduced long-term trends. In Fig. 7 we plot the global correction applied to the time series for each satellite with the corrected local reference time chosen to be 1200 noon for all observations. The choice of reference time has essentially no effect on the long-term trend series, since choosing a different time simply adds the same periodic signal with a constant offset to all satellites. An additional validation step based on residuals of intersatellite differences will be discussed in detail in section 4.

4. Intersatellite merging methodology

The final, and most crucial, step in constructing a composite time series of the MSU temperatures is that of merging the data from the nine instruments into a single time series of measured temperatures. Differences in the calibration offsets and nonlinear responses of the specific instruments, as well as residual errors stemming from an incomplete correction of the diurnal biases, lead to corresponding offsets in the measured brightness temperatures that must be removed before constructing a combined time series. An important factor, as noted previously, is the presence of strong correlations between the measured brightness temperature and the temperature of the hot calibration target (Christy et al. 2000, 2003; Prabhakara et al. 2000). The exact cause of this

so-called instrument body effect (IBE) is not known, but its presence in all of the MSU instruments strongly suggests that it stems from unresolved errors in the measurement and subsequent removal of radiometer nonlinearities. An error model for brightness temperature incorporating the IBE, first introduced by Christy et al. (2000), is

$$T_{\text{MEAS},i} = T_0 + A_i + \alpha_i T_{\text{TARGET},i} + \varepsilon_i, \qquad (1)$$

where T_0 is the true brightness temperature, A_i is the temperature offset for the ith instrument, α_i is a small "target factor" describing the correlation of the measured temperature with the temperature of the hot calibration target, $T_{\text{TARGET},i}$ is the target temperature anomaly for the ith satellite, and ε_i represents unresolved residual errors. Prabhakara et al. use a similar method, except that only a single target factor is used for all satellites (Prabhakara et al. 2000). In the following sections we show that different target factors α_i are necessary to accurately match the overlapping observations, confirming the earlier observations of CS. We also perform a detailed analysis of the uncertainty in the deduced values of the A_is and α_is, focusing on the strong error correlations and their ramifications for error estimates of long-term trends in brightness temperature.

a. Ocean-only merging

Our analysis of intersatellite merging is restricted to ocean-only observations. As discussed in the previous section, the diurnal cycle over the oceans is much smaller and smoother than over land, and is less likely to cause significant errors in either the retrieved values of the merging parameters or in the resulting merged time series.

Determination of the intersatellite merging parameters begins with pentad (5 day) averages of global brightness temperature for each field of view to reduce noise. We assume that merging parameters depend solely on the instrument, and is independent of geolocation and orbital node as tests using zonally varying merging parameters revealed little significant difference in the final trend statistics or merging parameters. Global oceanic pentad averages are determined from averages of 5° zonal pentad series, area weighted for each field of view separately over the latitude range from 85°S to 85°N. If the number of individual data points in any pentad fell below 95% of the median value for that zonal band, that pentad was discarded to guard against systematic nonuniform spatial sampling due to extended periods of missing data. The final global series presented here are averages over the central five fields of view, providing a global near-nadir pentad time series for each instrument.

For each pentad that includes valid averages from more than one satellite, we construct the following difference equation for each distinct pair of satellites for each pentad denoted by time t_n:

$$\begin{aligned} T_{\text{diff}}(t_n) &= T_{\text{MEAS},i}(t_n) - T_{\text{MEAS},j}(t_n) \\ &= A_i + \alpha_i T_{\text{TARGET},i}(t_n) - A_j - \alpha_j T_{\text{TARGET},j}(t_n) \\ &\quad + \varepsilon_i - \varepsilon_j. \end{aligned} \qquad (2)$$

The absence of an absolute external calibration reference requires us to choose a single baseline brightness temperature as the arbitrary reference offset; here we set $A_{NOAA\text{-}10}$ to be 0.0, leaving us with a system of many linear equations ($\sim$1200 overlapping pentads) in 17 unknowns (eight offsets + nine target factors). We solve the resulting system of equations using multiple linear regression, simultaneously minimizing the sum of the squared differences between satellites.

Figure 8 presents the results of this merging calculation. The fit does an excellent job of accounting for not only the large intersatellite offsets, but also for the significant seasonal-scale fluctuations, which are highly correlated with the target temperature differences. These fluctuations are especially large for satellite pairs that include data from *NOAA-11* after 1992, when the target temperature for *NOAA-11* began to experience large variations due to its drift to later crossing times. With the regression coefficients from this fit, we are able to generate a complete merged time series of brightness temperatures from all nine instruments simply by averaging together the individual pentad data corrected by application of the regressed offset and target, followed by a median filter to remove outliers.

b. Estimating errors in trends

When computing trends, it is critical to estimate the uncertainty in the resulting estimates, and to ascertain the specific merging parameters that contribute the most to the final error budget. The covariance matrix derived from our multiple regression analysis contains the needed information about both the errors in each parameter and the correlations between errors in different parameters. We use a Monte Carlo approach to estimate the uncertainties in the trend along with the sensitivity of the trend to changes in individual parameters. We would like to stress that the error estimates we obtain in this way are only estimates of the internal statistical errors, and do not include possible errors due to error in the diurnal adjustments, or undetected instrument drift.

The covariance matrix is dependent on our estimate of the measurement errors for the intersatellite differences, estimated by analyzing the distribution of the after-the-fit residuals. We approximate the random errors in the intersatellite differences by the standard deviation of the residuals for all the satellite pairs combined, presented in Table 1. Since the residuals exhibit a significant lag-1 (pentad) autocorrelation ρ of $\sim$0.40, we adjust the final uncertainties in offsets, target factors, and trends by $\sqrt{(1 + \rho)/(1 - \rho)} = 1.52$ to account for the reduction in degrees of freedom implied by this autocorrelation.
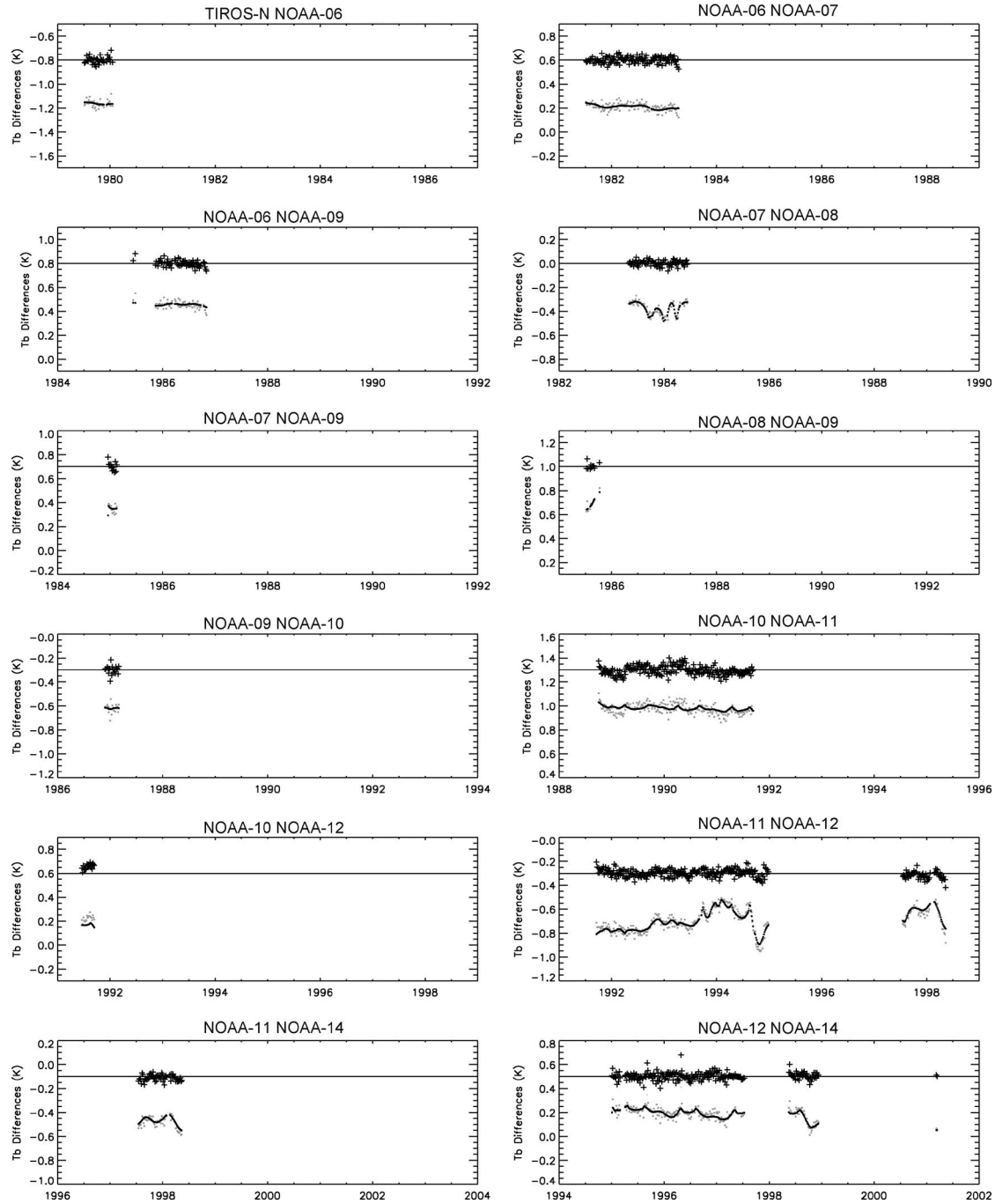
FIG. 8. Results of the satellite merging calculation, plotted separately for each satellite pair. In each plot, gray dots represent oceanic pentad averages of brightness temperature differences between pairs of satellites, and the black dots are a fit to the differences, using only both constant satellite offsets and target factors. The black crosses are the residuals to the fit, offset for clarity. The line through the black crosses is a horizontal line at zero residual to guide the eye.

To perform our Monte Carlo analysis, we generated an ensemble of 30 000 sets of 17 correlated random deviates with statistical properties consistent with the covariance matrix. These correlated deviates were added to the fitted parameters to obtain an ensemble of 30 000 "noisy" sets of merging parameters. We then calculated

combined T_b time series corresponding to each noisy set and performed linear regression on the resulting noisy time series to obtain a "noisy" set of trends, the standard deviation of which is used in our estimate of the overall trend error.

While this procedure yields a consistent estimate of

TABLE 1. Estimated errors in intersatellite pentad differences.

Data subset	Std dev of residuals to fit (K)
Ocean only	0.033
Land only	0.064
Ocean and land	0.031

the error in the trend, it does not provide any insight into the sensitivity of the trend to the choice of any one particular merging parameter, nor does it establish which pairs of satellites have the most critical overlap regions. In order to understand the individual contributions to the overall error, we performed a regression virtually identical to that described above, but using the intersatellite temperature differences as the prognostic variable, enabling us to separate out the individual contributions of each overlap pair to the overall trend. The resulting covariance matrix is used to create sets of noisy intersatellite differences and target temperature multipliers, as previously described, and the sensitivity of the final trend to each individual parameter determined from linear regression to the simulated trends.

The presence of large off-diagonal terms in the covariance matrix of merging parameters, plotted in Fig. 9, demonstrates the presence of strong correlations between certain pairs of parameters. In particular, it is notable that both the *NOAA-9* offset and the *NOAA-9* target temperature factor are relatively poorly constrained and strongly interdependent. The intersatellite difference sensitivity analysis presented in Table 2 shows that most of the intersatellite differences are well defined, with standard deviations below 0.005 K. Notable exceptions are those parameters involving *NOAA-9–NOAA-10, NOAA-8–NOAA-9,* and *NOAA-7–NOAA-9* overlap, with standard deviations in the range of >0.01 K. The overall trend is also quite sensitive to the *NOAA-9–NOAA-10* offset. The combination of large error and large sensitivity leads to correspondingly large contributions to the trend error, with the contribution from the *NOAA-9–NOAA-10* overlap contributing more than twice the error of any other overlap. In Table 3,
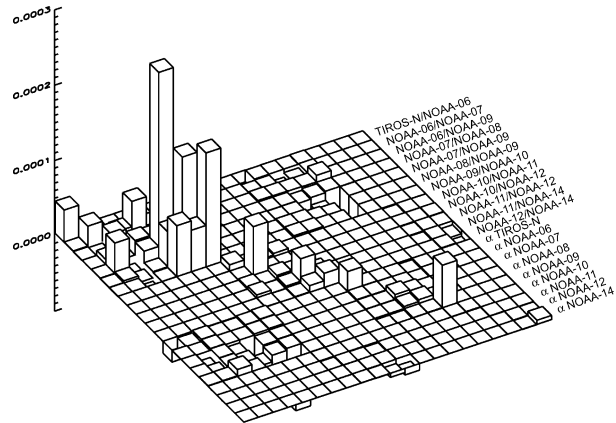

FIG. 9. Lego plot of the covariance matrix for ocean-only data. The first 12 parameters, starting from the upper-left corner of the surface, correspond to the intersatellite differences, shown in the same order as in Table 2. The last nine correspond to the target multipliers. The on-diagonal elements are the variance of each parameter, so large values show those parameters that are poorly determined. Large positive or negative off-diagonal terms indicate strong correlations between the parameters. The differences involving *NOAA-9* and the *NOAA-9* target temperature are both poorly constrained and strongly correlated.

we present results of a similar sensitivity analysis for the target temperature factors. Again, the parameters are all well defined except for that associated with *NOAA-9,* which contributes to the overall trend an error almost 3 times the contribution of any other target factor.

Based on this sensitivity analysis, the weakest link in the satellite merging analysis appears to be the *NOAA-9–NOAA-10* overlap, since it is critically located in the center of the time series and spans only 19 pentads. The value of the *NOAA-9–NOAA-10* difference is also strongly correlated with the *NOAA-9* target factor due to the nearly monotonic increase in *NOAA-9*'s target temperature during its lifetime, making this target temperature factor critical for connecting the *NOAA-6–NOAA-9* overlap with the later *NOAA-9–NOAA-10* overlap.

TABLE 2. Intersatellite sensitivity analysis.

Satellite 1	Satellite 2	No. of overlapping pentads	Intersatellite difference (K)	Std dev of intersatellite difference (K)	Sensitivity of trend (dTrend/dDiff) (decade^{-1})	Estimated contribution to std dev of trend (K decade^{-1})
TIROS-N	*NOAA-6*	35	−1.1421	0.0096	0.094	0.0009
NOAA-6	*NOAA-7*	120	0.1562	0.0076	−0.049	0.0004
NOAA-6	*NOAA-9*	63	0.4326	0.0068	0.068	0.0005
NOAA-7	*NOAA-8*	72	−0.3659	0.0064	0.042	0.0005
NOAA-7	*NOAA-9*	12	0.2534	0.0232	0.194	0.0045
NOAA-8	*NOAA-9*	11	0.6461	0.0174	0.310	0.0053
NOAA-9	*NOAA-10*	19	−0.6136	0.0182	0.616	0.0112
NOAA-10	*NOAA-11*	213	0.8771	0.0046	0.726	0.0033
NOAA-10	*NOAA-12*	18	0.2192	0.0119	0.094	0.0012
NOAA-11	*NOAA-12*	311	−0.7132	0.0031	0.662	0.0020
NOAA-11	*NOAA-14*	57	−0.6064	0.0081	0.385	0.0031
NOAA-12	*NOAA-14*	283	0.1328	0.0058	0.521	0.0030

TABLE 3. Target temperature factor sensitivity analysis.

Satellite	Target temperature factor α	Std dev of α	Sensitivity of trend (dTrend/dα) (K decade^{-1})	Contribution of std dev of trend (K decade^{-1})
TIROS-N	+0.0023	0.0071	−0.001	0.0000
NOAA-6	+0.0005	0.0014	1.689	0.0024
NOAA-7	+0.0166	0.0025	−0.045	0.0001
NOAA-8	+0.0300	0.0030	−0.105	0.0003
NOAA-9	+0.0195	0.0092	−0.789	0.0072
NOAA-10	+0.0032	0.0012	−0.329	0.0004
NOAA-11	+0.0277	0.0009	−2.756	0.0024
NOAA-12	+0.0059	0.0006	2.450	0.0015
NOAA-14	+0.0289	0.0030	−0.958	0.0029

c. Land-only and global merging

We now address the extension of the merging procedure for ocean-only data to the land-only and land-and-ocean brightness temperatures. In merging these datasets, we use the target factors from our ocean-only analysis. We have greater confidence in our ability to determine these factors accurately for two reasons. First, there is significantly greater variability of the globally averaged brightness temperatures over land, due to diurnal effects and uneven sampling of land regions with different brightness temperatures between separate 5-day averaging periods. This leads to increased noise in the global land pentad averages, which in turn increase the error in the fitted parameters. Second, the values of the target factors deduced are influenced by the sampling of the diurnal cycle along with the details of our diurnal correction. These corrections are larger, and therefore likely to have larger errors, over land. This is especially important for *NOAA-11*, where there is a long-term drift in the target temperatures and a long-term diurnal correction of approximately the same shape. By using the oceanic values for the target factors, both problems are avoided. We also expect the target factors to be the same over land as over ocean, since the error in the satellite measurements and the time dependence of the target temperature should be unaffected by whether the instrument is viewing a land or ocean scene. In contrast, we do not necessarily expect the satellite offsets to be

TABLE 4. Offsets and nonlinear target multipliers derived from regression to the global average land and ocean pentad series for MSU channel 2, using the central five FOVs.

| Satellite	Ocean-only offsets (K)	Land-only offsets (K)	Land and ocean	Target multipliers
TIROS-N	−1.3218	−1.3554	−1.3244	+0.0023
NOAA-6	−0.1798	−0.2392	−0.1915	+0.0005
NOAA-7	−0.3393	−0.3700	−0.3438	+0.0166
NOAA-8	0.0266	−0.0472	+0.0078	+0.0300
NOAA-9	−0.6117	−0.5515	−0.5922	+0.0195
NOAA-10	0.0000	0.0000	0.0000	+0.0032
NOAA-11	−0.8829	−0.8436	−0.8721	+0.0277
NOAA-12	−0.1672	−0.1301	−0.1553	+0.0059
NOAA-14	−0.2898	−0.1814	−0.2554	+0.0289
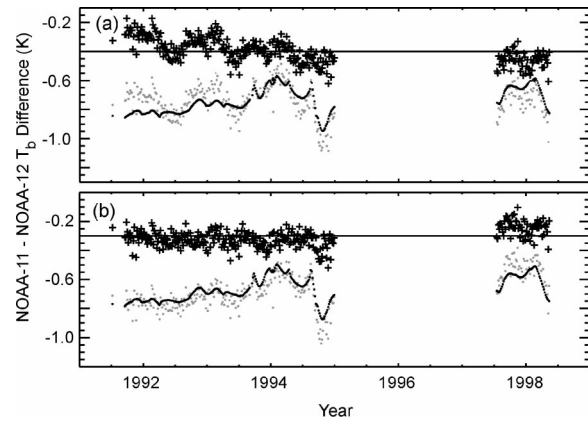
FIG. 10. Results of the satellite merging calculation analogous for the *NOAA-11–NOAA-12* overlap period. The gray dots are the *NOAA-11–NOAA-12* differences. The black dots represent the fit to the differences using the ocean-only target multipliers. The black crosses are the after-the-fit residuals, offset so that the horizontal line is zero. (a) Merger performed without the diurnal correction. Note the overall slope of the residuals in the 1992–95 time period due to the drift in local crossing time of *NOAA-11*. (b) Merger performed using the diurnal correction. Note the marked reduction in the slope and the seasonal cycle in the residuals. This provides another check on the validity of the CCM3-based diurnal correction.

identical, since the different data subsets sample different parts of the diurnal cycle (which may not be perfectly removed), and there may be unaccounted for residual nonlinear instrumental effects, leaving scene-temperature dependence in the average offset. The data confirm our suspicions; offsets must be recalculated for each data subset to avoid small but significant (typically <0.04 K) discontinuities in the residuals to the merging fit. Ocean-only, land-only, and land and ocean offsets for each instrument are shown in Table 4.

In Fig. 10, we show the results of a merge analogous to those shown in Fig. 8, applied to the land-only data. Measurements whose altitude exceeds 1500 m at the center of the measurement footprint are excluded from the global land-only merging process to reduce the effects of surface emission. We only plot the *NOAA-11–NOAA-12* overlap, since the effects of the diurnal cycle are the most important for this overlap. During the 4-yr overlap period from 1991 to 1995, the ascending LECT for *NOAA-11* drifted from 1500 LT, just after the peak of the diurnal cycle, to 1930 LT, experiencing significant diurnal cooling. In contrast, over the same period the *NOAA-12* crossing times were nearly stable, contributing little diurnal temperature drift. The effect of this differential drift in LECT is an apparent cooling of the *NOAA-11* global averages relative to *NOAA-12*, giving rise to a slope in the residuals shown in Fig. 10a.

When we repeat the calculation using data corrected for the diurnal cycle with the correction outlined in section 3, we obtain the results shown in Fig. 10b. From the figure it is apparent that the *NOAA-11–NOAA-12* slope during 1991–95 is mostly eliminated. Seasonal-scale oscillations in the *NOAA-11–NOAA-12* residuals
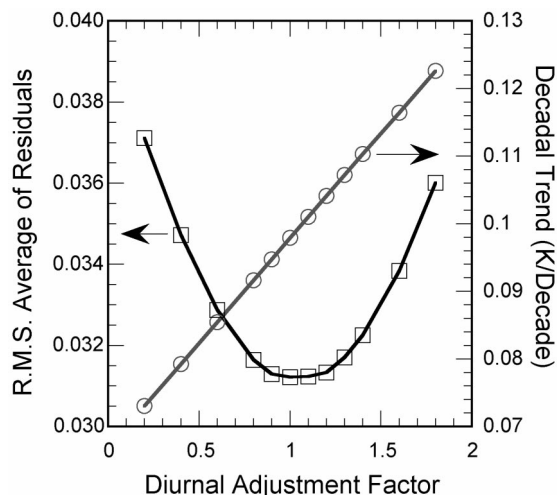
FIG. 11. The dependence of the rms fit residuals on multiplicative scaling of the diurnal correction derived from the CCM3 model (squares, scale on left), and the derived decadal trend plotted for each scaling factor (circles, scale on right).

have also been reduced (but not eliminated) by the diurnal correction. These seasonal-scale fluctuations represent a potential source of uncorrected systematic error, since they could, if present in the critical *NOAA-9–NOAA-10* overlap interval, lead to errors in the corresponding brightness temperature offset.

To test the possibility that our diurnal correction is over- or undercompensating, we performed an analysis of the dependence of the global temperature trend on a linearly scaled version of the initially determined correction term. As shown in Fig. 11, the trend itself shows a linear dependence on the scaled diurnal correction, while the residual rms goodness-of-fit measure shows a smooth evolution toward a minimum near a scaling factor of 1.0. This provides further support for the argument that our model-based diurnal signal is accurately representing the overall global diurnal contribution to the overall MSU time series.

5. Trends in MSU midtropospheric temperatures

Given that much of the interest in the MSU temperature time series centers on long-term climatological trends, we focus on these in the following discussion. Note that the intersatellite offsets are, in a number of cases, sufficiently large that to neglect them would noticeably impact the analysis of seasonal or interannual fluctuations. For this reason, we believe that the reanalyzed data will be of interest not only to researchers in climate change but also to those studying other phenomena such as surface–atmosphere coupling or temperature impacts of volcanic aerosols.

In Fig. 12 we plot monthly average (85°S–85°N) time series of the MSU2 brightness temperature anomaly for three different subsets of the data: (a) ocean only, (b) land only, and (c) both land and ocean. The lower por-
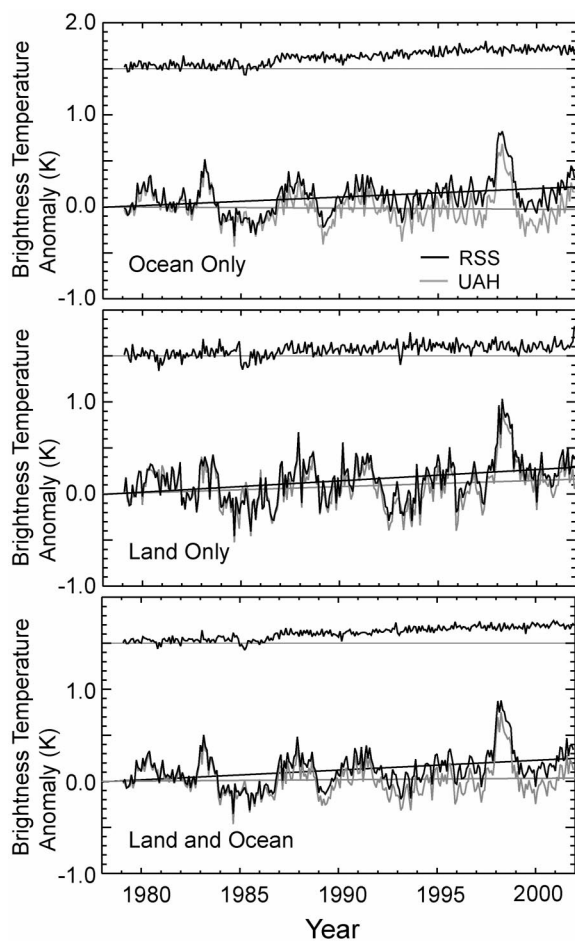

FIG. 12. Trends in global MSU channel 2 brightness temperatures. (a) Ocean-only global time series. In the pair of traces, the black trace is the monthly time series we found, while the gray trace corresponds to the ocean-only time series from Christy and Spencer, version 5.0. The black line is a linear fit to our time series, and a gray line is a fit to the Christy and Spencer time series. The top trace shows a difference time series (T2 RSS − T2 CS), offset by 1.5 K. Note that most of the difference between these two datasets occurs during the 1985–87 time period when *NOAA-9* was active. (b) Same as in (a) except for land-only observations. (c) Same as in (a) except for land and ocean data combined.

tion of each panel has Remote Sensing Systems' (RSS) reanalyzed data plotted in black, with the equivalent series from CS (version 5.0) shown in gray for comparison. Difference curves for the two analyses are plotted in the upper portion of the panel. While the interannual fluctuations in temperature reveal an extremely high degree of correlation in all three cases, it is apparent from the difference curves that the linear trends for the two datasets differ significantly. The origins of this discrepancy will be discussed in depth in section 6.

Table 5 presents the values for regressed linear trends for the RSS dataset, both with and without the diurnal correction applied, for the CS dataset corresponding to each of the three plotted subsets, and the global trend value for the Prabhakara et al. dataset over the time

period 1979–99. Our trend values are provided with 2-σ error bounds calculated using the Monte Carlo procedure outlined in section 3, and with the corresponding rms value of the fit residuals. Over the ocean, where diurnal drift is unlikely to have a significant influence on the series, we observe a warming trend of 0.099 K decade^{-1}, in clear contrast with the slight cooling trend (-0.011 K decade^{-1}) derived by CS. As anticipated, our warming trend only decreases by 0.008 K decade^{-1} when the diurnal correction is not applied.

Over land we note a significantly increased sensitivity to the diurnal correction, with the uncorrected warming of 0.023 K decade^{-1} increased significantly to 0.087 K decade^{-1} by its application. The CS value of 0.050 K decade^{-1} warming is closer to our trend than the ocean-only observations, leading to a CS land $-$ ocean differential of more than twice that found in the RSS data. Our global trend for both land and ocean combined is 0.097 K decade^{-1}, essentially the area-weighted average of the land and ocean data, and shows nearly 0.1 K decade^{-1} greater warming than the corresponding CS analysis. The relatively small sensitivity of the land and ocean trend to the application of the diurnal correction indicates that errors in the correction procedure will have a small effect on the deduced global trends.

The spatial distribution of trends for the RSS and CS data, shown in Fig. 13, provides a method of evaluating in more detail the characteristic fingerprint of change in the MSU2 observations. Monthly anomalies were computed using target factors derived from the ocean-only data and offsets determined from the combined land and ocean dataset, providing a set of 2.5° maps for the entire MSU channel 2 dataset. Corresponding monthly time series were generated for each grid cell from the anomaly maps, with trends for each series determined by simple linear regression (Fig. 13a). An identical procedure was applied to the CS monthly anomaly data, providing a comparable map of their trends (Fig. 13b). The difference between the RSS and CS trends is shown in Fig. 13c. Apparent in the CS trend map is an enhanced longitudinal smoothness, an effect that probably stems from their zonal interpolation methods (Spencer and Christy 1992a), accompanied by a corresponding decrease in meridional smoothness that
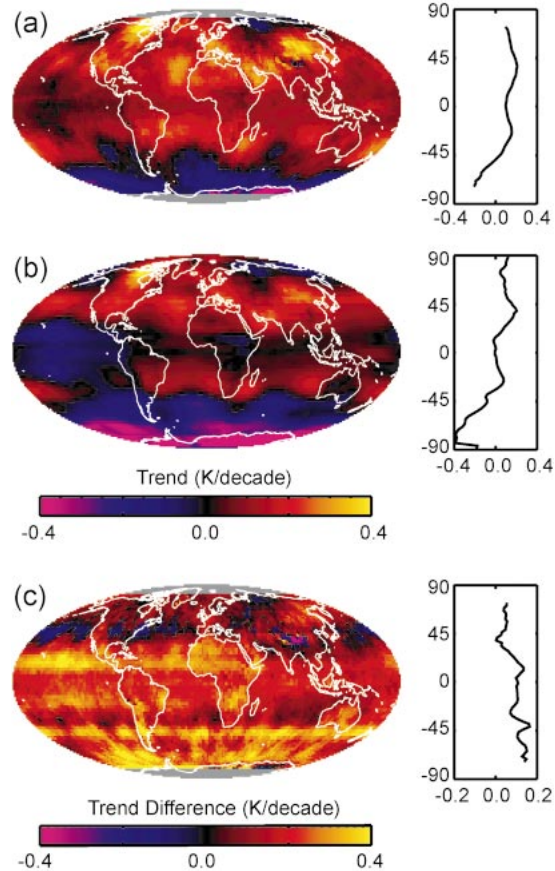

FIG. 13. Color-coded map of global MSU channel 2 brightness temperature trends for the period 1979–2001 for the (a) RSS and (b) CS version 5.0 datasets. (c) The spatial distribution of the trend differences (RSS $-$ CS) is plotted on the same scale as in (a), (b).

may be attributable to their use of zonally dependent merging coefficients.

Both the RSS and CS trend maps show significant warming in the Northern Hemisphere, and their zonal profiles seem quite similar in shape despite the global trend offset of 0.1 K decade^{-1}. However, examination of the zonal difference map in Fig. 13c reveals a strong latitude dependence of the offset, with a clear upward step between 30°N and the equator. In the high northern

TABLE 5. Long-term trends in the MSU2 brightness temperature anomalies for 1979–2001. The Prabhakara et al. value is over the period fron 1979–99, our value for this time period is 0.095 K decade^{-1}.

	Analysis method	Trend (K decade^{-1})	Rms of residual (K)
Ocean only	Diurnally corrected	0.098 ± 0.028	0.033
	No diurnal correction	0.091 ± 0.030	0.034
	Spencer and Christy, version 5.0	-0.011	
Land only	Diurnally corrected	0.087 ± 0.046	0.064
	No diurnal correction	0.023 ± 0.046	0.077
	Spencer and Christy, version 5.0	0.050	
Global	Diurnally corrected	0.097 ± 0.028	0.031
	No diurnal correction	0.067 ± 0.028	0.040
	Spencer and Christy, version 5.0	0.009	
	Prabhakara et al.	0.13	

TABLE 6. Summary of important differences between the RSS and CS methods.

	RSS	CS
Diurnal adjustment: origin	Derived using hourly output from the CCM3 climate model, and a radiative transfer model	Derived using observed cross-scan differences measured by the MSU instruments
Diurnal adjustment: methodology	Adjustments all made to a single reference time (noon, local time)	Adjustments made to different reference times for each satellite (local time of first observation for each moth of instrument operation)
Determination of target factors	All valid 5-day averages with simultaneous observations for two or more satellites used in least squares regression procedure	Only long-term periods of satellite overlap used; some target factors set to zero if their improvement to the intersatellite differences are insufficient to warrent use
Determination of intersatellite offsets	Determined in a unified way during the regression procedure for determining target factors	Determined using a single path or "backbone" that links together the various satellites
Smoothing before target factor determination	5-day averages	60–120-day averages

latitudes where large regions of significant warming over Siberia and northeastern Canada are observed, and where the most of the high quality radiosonde observations used in validations of the CS dataset reside, the two datasets are in generally good agreement, both in terms of the characteristic spatial patterns and in absolute trend magnitude. Two notable exceptions are over northern Africa, where we observe significant warming relative to CS, and the Himalayas, where we see much less warming than CS, perhaps due to differences in the details of our respective diurnal temperature corrections.

The Tropics and southern high latitudes, in contrast, show significant biases between the RSS data and the CS data. Both datasets reveal significant cooling in the southern oceans and over Antarctica, but the magnitude of this is much smaller in our analysis. Elsewhere, with the prominent exception of the equatorial Pacific where the CS data show strong cooling trends in contrast to the very slight warming seen in our data, the results appear to differ by an almost constant offset. These results make it clear that any attempts to validate global MSU temperature trend data with radiosonde or other in situ observations must take great care to sample the globe as uniformly as possible (Hurrell et al. 2000). Such efforts may be stymied by the preponderance of observing stations in the Northern Hemisphere and the paucity of reliable observations of any sort over the southern oceans.

6. Discrepancies between the RSS and CS analyses

There are a number of differences in methodology between RSS and CS that may contribute to the observed discrepancies in the deduced trends. In Table 6, we summarize differences between the two methods that could significantly change the long-term global time series. First, there are significant differences in the origin and application of the adjustments used to correct for diurnal drift. We calculate the diurnal cycle for each $2.5° \times 2.5°$ grid point using a GCM (CCM3), and then validate it in a number of ways using consistency with MSU data. Christy and Spencer account for diurnal drifts by considering systematic cross-scan differences between measurements taken at slightly different local times (Christy et al. 2000, 2003), thus deducing the effect of diurnal drift directly from the MSU measurements themselves. Despite this difference, on a *global* scale, the two adjustments are in good agreement with each other. When we reprocess our data using the CS diurnal correction, the global trend is decreased by only 0.006 K decade^{-1}, less than 7% of the total difference between our results.

A more important difference between our methodologies is the way in which we determine the intersatellite merging parameters. We use a unified approach where each overlapping pentad average is treated with equal weight to determine both the target factors and the intersatellite offsets. The equal weighting of each 5-day overlap serves to deemphasize periods of short overlap without ignoring them altogether. Christy et al. (2000, 2003) impose a minimum time period over which an overlap must occur before it can be taken into account to help determine the merging parameters. This leads CS to discard the *TIROS-N–NOAA-6, NOAA-7–NOAA-9, NOAA-8–NOAA-9, NOAA-9–NOAA-10,* and *NOAA-10–NOAA-12* overlaps when determining their target factors. Their intersatellite offsets are then determined by evaluating the mean difference between coorbiting satellites utilizing a single path that connects all the satellites in question.

Ultimately these differences in analytical methodology result in significantly different values for the *NOAA-9,* and to a lesser extent the *NOAA-11,* target factors. When we implement the CS merging procedure and diurnal correction, but use our 5-day land-and-ocean pentad-average data, we obtain a value for the *NOAA-9* target factor of 0.075, almost as large as the value of 0.095 reported by CS. As we noted in section 3, the bulk of the trend discrepancies between the RSS and CS analyses of the MSU2 dataset arises from a short, nearly steplike transition in the time period between 1985 and 1987, corresponding to the interval during
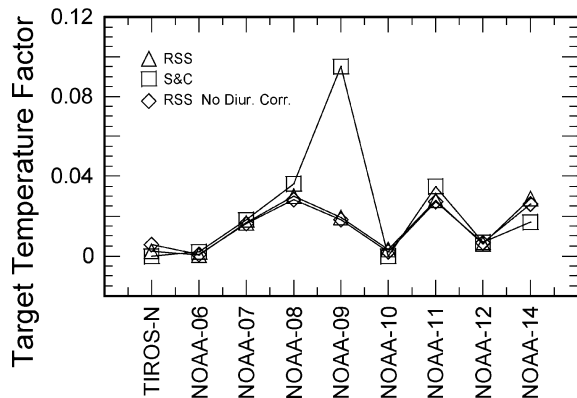
FIG. 14. Comparison of target temperature factors. The two sets of RSS derived target temperature factors were calculated using ocean-only data. The Christy and Spencer version 5.0 target temperature factors were obtained using both land and ocean data. Note the general agreement between the RSS values and the CS values, except for *NOAA-9.*

which *NOAA-9* constituted a critical link between the earlier and later instruments, and a slow ramp from 1991 to 1995, corresponding to the large drift in LECT for *NOAA-11,* causing both a large diurnal drift and large fluctuations in the calibration target temperatures, which amplify the relatively small differences in *NOAA-11* target factors and in our diurnal adjustment procedures. Figure 14 shows the target factors for all satellites for two different versions of our methodology, one with and one without any added diurnal corrections, along with corresponding factors from Christy et al. (2003). Except for *NOAA-9,* almost all of our target factors are also in good agreement with those found by CS, and in rough agreement with the single, satellite-independent target factor of 0.03 found by Prabhakara et al. (2000).

The CS target coefficient calculation focuses on reducing low-frequency differences during the overlapping periods. The use of the CS coefficient for *NOAA-9* reduces the intersatellite trend between *NOAA-6* and *NOAA-9* seen in Fig. 8 from 0.04 to -0.01 K yr^{-1}, but at the expense of significantly increasing other intersatellite difference trends, especially those ignored by Christy and Spencer.

In order to quantify the effect of the differing *NOAA-9* target factors, we exactly reproduced our ocean-only merging procedure with the sole exception that we fix the value of the *NOAA-9* target factor to the CS value of 0.095; the trend value then becomes 0.022 K decade^{-1}, a difference of 0.073, indicating that differences in this one target factor are responsible for a large fraction of the overall difference between these analyses. This difference is slightly larger than would be expected (0.060) from our Monte Carlo analysis presented above. In this case, the other target factors are held fixed, while in the Monte Carlo case, they vary according to their respective correlations with the target factor in question. When CS perform a similar study using their data and

RSS target coefficients, they report a difference of only 0.05 K decade^{-1} (J. R. Christy 2003, personal communication).

Another difference between our analyses and those of CS is in the amount of temporal smoothing performed before calculating merging parameters. We use pentad averages in our regression procedure, while CS use 60–120-day averages when calculating target factors. We reanalyzed our data after performing a 60-day running mean average on the global oceanic pentad averages. This resulted in small changes in our target factors that led to a decrease in the global trend from 0.098 to 0.096 K decade^{-1}.

7. Summary

We have performed a complete end-to-end reanalysis of the MSU channel 2 tropospheric temperature data, including extensive geolocation and data quality control measures; corrections for incidence angle variation, orbit decay, and satellite roll error; a new diurnal correction methodology based on GCM simulations of the diurnal cycle; and a multiple linear regression merging algorithm that incorporates all available overlapping observations in a uniform and self-consistent error model. Monthly maps of mean brightness temperature from our analysis are available via the World Wide Web (http://www.remss.com/msu/msu_browse.html).

As a diagnostic criterion, we compare long-term decadal trends derived from our dataset with trends in the Christy and Spencer (1995) dataset over an identical interval, revealing a difference of approximately 0.09 K decade^{-1}, with our analysis warming significantly more than theirs. On shorter timescales, the two sets of observations are virtually indistinguishable. While all of the corrections are important, the primary source of disagreement is in the nonlinear target factor for the *NOAA-9* instrument. This platform ties together the preceding and successive instruments through an extremely short 17-pentad overlap period with *NOAA-10,* making the final series quite sensitive to its merging parameters. For this particular instrument the fractional contribution of the correction for nonlinearity made by the target multiplier in the Christy and Spencer analysis is ~10%, more than 5 times our corresponding multiplier and more than 3 times larger than the multiplier for any other instrument. By itself, this difference is responsible for ~0.07 K decade^{-1} of the overall difference in the decadal trends, with the remainder arising from our differing treatments of the diurnal temperature cycle and differences in the *NOAA-11* target factor.

A number of studies of tropospheric temperatures as measured by radiosondes have found 0.1–0.2 K decade^{-1} less warming than we see in our results (Angell 2000; Lanzante et al. 2003b; Parker et al. 1997). Recent studies have found that the trends determined for individual radiosonde observation stations can vary by more than 0.1 K decade^{-1} depending on adjustments

made for temporal inhomogeneities in instrumentation or observing practice (Gaffen et al. 2000; Lanzante et al. 2003b), and differences in derived trends between different versions of the same global datasets can change by almost this amount (Santer et al. 1999). Based on these results we think it is inappropriate to use radiosonde comparisons as the single method for validating satellite-derived temperature trends, and studies, such as ours, that are primarily based on internal consistency should be considered on equal footing.

REFERENCES

Angell, J. K., 2000: Tropospheric temperature variations adjusted for El Niño, 1958–1998. *J. Geophys. Res.,* **105,** 11 841–11 849.

Christy, J. R., and R. W. Spencer, 1995: Assessment of precision in temperatures from the microwave sounding units. *Climatic Change,* **30,** 97–102.

——, ——, and E. S. Lobl, 1998: Analysis of the merging procedure for the MSU daily temperature time series. *J. Climate,* **11,** 2016–2041.

——, ——, and W. D. Braswell, 2000: MSU tropospheric temperatures: Dataset construction and radiosonde comparisons. *J. Atmos. Oceanic Technol.,* **17,** 1153–1170.

——, ——, W. B. Norris, W. D. Braswell, and D. E. Parker, 2003: Error estimates of version 5.0 of MSU–AMSU bulk atmospheric temperatures. *J. Atmos. Oceanic Technol.,* **20,** 613–629.

Gaffen, D., M. Sargent, R. Habermann, and J. Lanzante, 2000: Sensitivity of tropospheric and stratospheric temperature trends to radiosonde data quality. *J. Climate,* **13,** 1776–1796.

Gentemann, C. L., C. J. Donlon, A. Stuart-Menteth, and F. J. Wentz, 2003: Diurnal signals in satellite sea surface temperature measurements. *Geophys. Res. Lett.,* **30,** 1140, doi:10.1029/2002GL016291.

Hansen, J., H. Wilson, M. Sato, R. Ruedy, K. Shah, and E. Hansen, 1995: Satellite and surface temperature data at odds? *Climatic Change,* **30,** 103–117.

——, R. Ruedy, M. Sato, M. Imhoff, W. Lawrence, D. Easterling, T. Peterson, and T. Karl, 2001: A closer look at the United States and global surface temperature change. *J. Geophys. Res.,* **106,** 23 947–23 963.

Hoots, F. R., and R. L. Roehrich, cited 2003: Spacetrack Rep. 3. [Available online at www.celestrak.com/NORAD/documentation/spacetrk.pdf.]

Houghton, J. T., Y. Ding, D. J. Griggs, M. Noguer, P. J. van der Linden, X. Dai, K. Maskell, and C. A. Johnson, Eds., 2001: *Climate Change 2001: The Scientific Basis*. Cambridge University Press, 881 pp.

Hurrell, J. W., S. J. Brown, K. E. Trenberth, and J. R. Christy, 2000: Comparison of tropospheric temperatures from radiosondes and satellites: 1979–98. *Bull. Amer. Meteor. Soc.,* **81,** 2165–2178.

Kidwell, K. B., cited 1998: NOAA polar orbiter data users guide. National Climatic Data Center, 417 pp. [Available online at http://www2.nodc.noaa.gov/docs/podug/.]

Kiehl, J. T., J. J. Hack, G. B. Bonan, B. A. Boville, B. P. Briegleb, D. L. Williamson, and P. J. Rasch, 1996: Description of the NCAR Community Climate Model (CCM3). National Center for Atmospheric Research Tech. Note NCAR/TN-420+STR, Boulder, CO, 152 pp.

Lanzante, J., S. Klein, and D. Seidel, 2003a: Temporal homogenization of monthly radiosonde temperature data. Part I: Methodology. *J. Climate,* **16,** 224–240.

——, ——, and ——, 2003b: Temporal homogenization of monthly radiosonde temperature data. Part II: Trends, sensitivities, and MSU comparison. *J. Climate,* **16,** 241–262.

Mears, C. A., M. Schabel, F. J. Wentz, B. D. Santer, and B. Govindasamy, 2002: Correcting the MSU middle tropospheric temperature for diurnal drifts. *Proc. Int. Geophysics and Remote Sensing Symp.,* Vol. III, Toronto, ON, Canada, IEEE Geophysics and Remote Sensing Society, 1839–1841.

Mo, T., 1995: A study of the microwave sounding unit on the *NOAA-12* satellite. *IEEE Trans. Geosci. Remote Sens.,* **33,** 1141–1152.

——, M. D. Goldberg, and D. S. Crosby, 2001: Recalibration of the NOAA microwave sounding unit. *J. Geophys. Res.,* **106** (D10), 10 145–10 150.

Parker, D. E., M. Gordon, D. P. N. Cullum, D. M. H. Sexton, C. K. Folland, and N. Rayner, 1997: A new global gridded radiosonde temperature data base and recent temperature trends. *Geophys. Res. Lett.,* **24,** 1499–1502.

Prabhakara, C., J. R. Iacovazzi, J.-M. Yoo, and G. Dalu, 1998: Global warming deduced from MSU. *Geophys. Res. Lett.,* **25,** 1927–1930.

——, ——, ——, and ——, 2000: Global warming: Evidence from satellite observations. *Geophys. Res. Lett.,* **27,** 3517–3520.

Santer, B. D., J. J. Hnilo, T. M. L. Wigley, J. S. Boyle, C. Doutriaux, M. Fiorino, D. E. Parker, and K. E. Taylor, 1999: Uncertainties in "observational" estimates of temperature change in the free atmosphere. *J. Geophys. Res.,* **104,** 6305–6334.

——, and Coauthors, 2000: Interpreting differential temperature trends at the surface and in the lower troposphere. *Science,* **287,** 1227–1232.

Shah, K. P., and D. Rind, 1995: Use of microwave brightness temperatures with a general circulation model. *J. Geophys. Res.,* **100** (D7), 13 841–13 874.

Spencer, R. W., and J. R. Christy, 1990: Precise monitoring of global temperature trends from satellites. *Science,* **247,** 1558–1562.

——, and ——, 1992a: Precision and radiosonde validation of satellite gridpoint temperature anomalies. Part I: MSU channel 2. *J. Climate,* **5,** 847–857.

——, and ——, 1992b: Precision and radiosonde validation of satellite gridpoint temperature anomalies. Part II: A tropospheric retrieval and trends during 1979–1990. *J. Climate,* **5,** 858–866.

Trenberth, K. E., and J. W. Hurrell, 1997: Response to "How accurate are satellite 'thermometers'?" *Nature,* **389,** 342–343.

Wallace, J. M., and Coauthors, 1999: *Reconciling Observations of Global Temperature Change.* National Academy Press, 85 pp.

Wentz, F. J., and M. Schabel, 1998: Effects of satellite orbital decay on MSU lower tropospheric temperature trends. *Nature,* **394,** 661–664.

——, and T. Meissner, 1999: AMSR ocean algorithm, version 2. Remote Sensing Systems RSS Tech. Rep. 121599A, 58 pp.